Microstructural basis for improved corrosion resistance and mechanical properties of fabricated ultra-fine grained Mg-Akermanite composites

Mehdizade, M.; Eivani, A. R.; Tabatabaei, F.; Jafarian, H. R.; Zhou, J.

DOI
10.1016/j.matchemphys.2022.126765

Publication date
2022

Document Version
Final published version

Published in
Materials Chemistry and Physics

Citation (APA)
Mehdizade, M., Eivani, A. R., Tabatabaei, F., Jafarian, H. R., & Zhou, J. (2022). Microstructural basis for improved corrosion resistance and mechanical properties of fabricated ultra-fine grained Mg-Akermanite composites. *Materials Chemistry and Physics*, *292*, Article 126765. https://doi.org/10.1016/j.matchemphys.2022.126765

Materials Chemistry and Physics 292 (2022) 126765

Contents lists available at ScienceDirect

Materials Chemistry and Physics

journal homepage: www.elsevier.com/locate/matchemphys

Microstructural basis for improved corrosion resistance and mechanical properties of fabricated ultra-fine grained Mg-Akermanite composites

M. Mehdizade [a], A.R. Eivani [a,*], F. Tabatabaei [a], H.R. Jafarian [a], J. Zhou [b]

[a] *School of Metallurgy and Materials Engineering, Iran University of Science and Technology, Tehran, Iran*
[b] *Department of Biomechanical Engineering, Delft University of Technology, Mekelweg 2, 2628, CD Delft, the Netherlands*

HIGHLIGHTS

- A new magnesium-based nanocomposite is developed by friction stir processing (FSP).
- Akermanite ceramic particles are used as reinforcing agents.
- Mechanical properties are enhanced due to grain refinement by FSP.
- Corrosion resistance is enhanced due to particle fragmentation and redistribution.
- Improved biocompatibility is observed due to the positive effects of Akermanite.

GRAPHICAL ABSTRACT

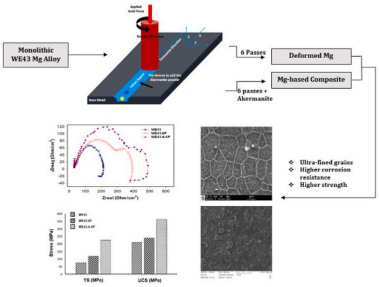

ARTICLE INFO

Keywords:
Magnesium
Akermanite
Corrosion
Composite
Friction stir processing

ABSTRACT

In the present research, a composite with a magnesium alloy (WE43) as the matrix and Akermanite as the bioactive and reinforcing agent was fabricated by friction stir processing (FSP), resulting in a microstructure with uniformly distributed fine grains, second-phase particles and micro-sized Akermanite particles. The effect of an addition of Akermanite to the alloy on the mechanical properties and corrosion resistance of the resulting composite was investigated. The compressive strength and ductility of the composite were found to be significantly higher than those of the monolithic WE43 alloy. The value of yield strength of the WE43 sample increased from 75 MPa up to 119 and 225 MPa for WE43-6P and WE43-A-6P samples, respectively. Also, the value of the ultimate compressive strength of the WE43 sample increased from 210 MPa up to 240 and 362 MPa for WE43-6P and WE43-A-6P samples, respectively. The value of elongation for WE43, WE43-6P, and WE43-A-6P samples were 4.5%, 16%, and 22%, respectively. The EIS test showed that the corrosion mechanism of WE43 sample is a combination of localized pitting and uniform corrosion, which shifted towards more uniform corrosion with higher corrosion resistance by applying FSP and adding Akermanite powder. The potentiodynamic polarization and in vitro immersion tests confirmed this finding, as evidenced by the increase in polarization resistance from 0.192 for the monolithic WE43 alloy up to 0.339 and 0.609 kΩ/cm^2 for WE43-6P and WE43-A-6P samples, respectively. The mass loss rate of the WE43 sample decreased from 20.82 to 10.13 mm per year for the WE43-A-6P sample after 312 h immersion in SBF solution. All tests approved that by applying FSP and adding Akermanite to WE43, the corrosion resistance in the SBF solution could be significantly enhanced.

---

* Corresponding author.
E-mail address: aeivani@iust.ac.ir (A.R. Eivani).

https://doi.org/10.1016/j.matchemphys.2022.126765
Received 25 May 2022; Received in revised form 6 September 2022; Accepted 11 September 2022

1. Introduction

Magnesium is a unique material for biomedical applications in view of its biocompatibility, biodegradability and high strength to density ratio. Considerable similarities of magnesium and its alloys to natural bone in mechanical properties and density, as well as their contributions to bone growth, have made magnesium an interesting candidate for orthopedic applications [1,2]. Human bone has a density of 1.8–2.1 g/cm^3 and elastic modulus of 3–20 GPa, being quite close to those of magnesium alloys, i.e., 1.74 to 2.9 g/cm^3 and 41–45 GPa, respectively [3]. This contracts the currently used orthopedic materials, such as titanium having a density of 4.4–4.5 g/cm^3 and elastic modulus of 110–117 GPa [4,5].

In addition to the mechanical properties, biodegradability is an extremely important merit of magnesium and, therefore, magnesium has attracted a lot of interest in recent years in developing metallic biodegradable medical devices, e.g., fracture fixation devices. On the other hand, biodegradation also means the deterioration of mechanical properties during the service time of such devices when damaged tissue heals by itself, accompanied by rapid hydrogen gas release. This may lead to the destruction of adjacent tissues. Like most of other metals in an aqueous medium, a protective layer of M(OH)n is formed, which is an insoluble protective layer of $Mg(OH)_2$ in the case of magnesium, thereby reducing the corrosion rate. Because of the presence of a high concentration of chloride in body fluids (approximately 150 mmol/l), $Mg(OH)_2$ will be degraded and converted into soluble $MgCl_2$, which results in unsuspended corrosion. Also, the MgO layer could be formed and act as protective film [6–11]. An addition of rare earth (RE) elements to magnesium has shown to have significant strengthening and anti-corrosion effects and therefore the alloying approach has been extensively taken to develop new biomaterials for orthopedic applications [12,13]. This approach however does not render solution to the weak bioactivity of magnesium, but making biocompatibility a more complex issue.

Adding bioactive ceramic powders like SiC [14,15], ZnO [16], Hardystonite [17], hydroxyapatite [18,19] etc., to magnesium is a less explored approach to enhance corrosion resistance and bioactivity simultaneously. In the field of bio-ceramics for bone tissue engineering, calcium silicate-based bio-ceramics have in recent years received a lot of attention because of their ability to promote osteoblast proliferation and differentiation relative to calcium phosphate-based bio-ceramics [4–6,20]. Among the silicate-based bio-ceramics, Akermanite has been found to have the most suitable release ratio of calcium, silicon, and magnesium ions into the body fluid, thereby playing an important physiological role in bone metabolism. Akermanite has been used as a coating on metal implants or bone tissue engineering scaffolds [20–22].

Friction stir processing (FSP), based on the principles of friction stir welding, is a relatively new method for material processing and for the fabrication of surface composites. Because the process involves severe plastic deformation, FSP of metals often results in significant grain refinement and enhanced physical and mechanical properties [17,23–30]. When FSP is applied to fabricate composites, additional benefits can be gained [31,32]. During FSP, severe plastic deformation results in stirring and vigorous plastic flow, facilitating the even distribution of reinforcing particles, in addition to heat generation causing dynamic recrystallization and significant grain refinement. By increasing the number of FSP passes, the uniformity of the particles in the following FSP passes increases, which is a reason for the enhancement of nucleation locations for new grains and inhibition of the grain growth. The process of FSP affects the microstructure and thickness of heterogeneous layers [14,33,34]. Recently, this technique has been successfully applied to create surface composites with fine-grained microstructures [15,35–38]. In the preceding research of the authors [23], it was found that severe plastic deformation during the FSP process caused redistribution of second-phase particles in the magnesium alloy WE43, in addition to significant grain refinement. By increasing FSP passes and resultant strains, the corrosion resistance and mechanical properties of the alloy were significantly improved [13,14,25,39,40].

The present research was aimed at enhancing the corrosion resistance and mechanical properties of the WE43 magnesium alloy further. To this end, Akermanite particles were added into the WE43 alloy to form a WE43-A composite. In addition to the characterization in microstructure and mechanical properties, the corrosion behavior of the fabricated composite was investigated by performing electrochemical impedance spectroscopy (EIS), potentiodynamic polarization (PP) and in vitro immersion tests.

2. Materials and experimental procedures

The WE43 magnesium alloy with the chemical composition given in Table 1 was used as the base material for preparing composite samples. An Akermanite ($Ca_2MgSi_2O_7$) powder was used as the bioactive and reinforcing agent. To minimize agglomeration of particles, the powder was dried, followed by dispersion in ethanol with the help of an ultrasonic stirrer.

FSP was conducted on the plate samples with a width of 50 mm and a length of 140 mm after annealing at 440 $^\circ C$ for 3 h. For inserting Akermanite particles into the WE43 plate, a groove with a width of 1 mm and a depth of 2 mm was machined along the length of the plate. The samples were cleaned, washed with soap and then degreased with acetone for 30 min and dried by blowing warm air. A schematic illustration of applied FSP and dimensions of FSP tool are shown Fig. 1. After inserting Akermanite particles into the groove, the groove was capped by a flat pin-less cylindrical tool with a diameter of 15 mm.

FSP was carried out using a tool with a shoulder diameter of 15 mm, a pin height of 2.5 mm and a pin diameter of 3.5 mm. The tool moving speed was 107 mm/min and the rotational speed was 1180 rpm [30,41]. The FSP process was repeated up to six passes, which was expected to lead to a uniform distribution of Akermanite particles in the composite. The schematics of process procedure is presented in Fig. 2. In this paper, the sample prior to FSP, the sample with six passes FSP and sample with six passes FSP + Akermanite powder are named WE43, WE43-6P and WE43-A-6P, respectively.

A TESCAN VEGA/XMU scanning electron microscope (SEM) was used to confirmed the sizes and morphology of Akermanite particles. SEM samples were ground to grit 1500 SiC sandpaper and polished. Subsequently, the samples were electro-etched in a 300 ml HNO_3 + 700 ml C_2H_5OH solution at 20 V and −35 °C. A HUVITZ HR3-TRF-P optical microscope (OM) and SEM equipped with an energy dispersive spectrometer (EDS) were used to investigate the microstructures of WE43, WE43-6P and WE43-A-6P samples. To reveal the microstructures in OM, samples were polished and etched in a reagent solution of 5 ml acetic acid +5 g picric acid +100 ml ethanol +10 ml distilled water. The grain structures of the samples were examined with an electron backscatter diffraction (EBSD) detector attached to the Philips XL30S FEG-SEM. The average grain size was determined using ImageJ analyzer. A DRON-8 X-ray diffractometer (XRD) with copper Kα radiation at 40 KV and 30 mA was used for the characterization of the Akermanite powder.

To evaluate the mechanical properties, uniaxial compression tests were conducted, according to the ASTM E9 standard. Cylindrical specimens with a diameter of 2 mm and a height of 3 mm were machined along the length. Before the tests, to minimize surface roughness and thus friction between the specimen and tool, both end sides of the specimens were mechanically polished. The tests were performed with a 50 kN SANTAM universal tensile/compression machine at a crosshead

Table 1
Chemical composition of the WE43 magnesium alloy used in this study.

Element	Mg	Zn	Y	Zr	Sc	Nd	Gd
Wt. %	Balance	0.08	3.72	0.41	1.47	2.13	1.11

speed of 0.5 mm/min.

Electrochemical Impedance Spectroscopy (EIS), Potentiodynamic Polarization (PP) and in vitro immersion tests were conducted by using an EG&G potentiostat-galvanostat device (model VersaSTAT4). A three-electrode cell with the sample as the working electrode, saturated calomel electrode (SCE) as the reference electrode and a platinum rode as the counter electrode is shown in Fig. 3. Before performing electrochemical analysis, all the samples with 10 mm^2 surface area were immersed in the simulated body fluid (SBF) solution for 20 min for stabilization. The electrochemical tests were performed at ambient temperature and repeated three times. The EIS tests were performed according to the ASTM B457-67 standard over an applied frequency range of 0.01–10^5 Hz at a 10-mV amplitude. The obtained results were fitted using the ZSimpWin 3.21 software. The potentiodynamic polarization tests were carried out, according to the ASTM G102-98-E1 standard at −250 mV below open circuit potential (OCP) up to reference electrode potential (SCE) at a scan rate of 1 mV/S. To investigate the corrosion behavior of the deformed Mg and the FSPed composite in physiological environments, in vitro immersion tests in SBF were conducted according to ASTM G31-72. Samples were in disc form with a dimeter of 1 cm and a thickness of 2 mm. During the immersion tests, samples were placed inside an incubator at 37 °C. After the immersion testes at different time points up to 312 h, the samples were washed with water, dried in air and weighed with ±0.001 g accuracy. The samples were cleaned using a solution composed of 180 g/L chromic acid and 2 g $AgNO_3$ to remove corrosion products, while leaving the samples intact. The samples were then weighed again to calculate the actual weight losses that had occurred during the immersion tests.

3. Results and discussion

3.1. Characteristics of the starting materials

Fig. 4 shows the microstructure of the as-annealed WE43 sample prior to FSP. It can be observed that the structure of the WE43 sample that had been annealed at 440 °*C* for 3 h was fully recrystallized with approximately equiaxed coarse grains. This could be attributed to the sufficiently high annealing temperature for long time, resulting in grain growth to values between 10 and 40 μm according to ASTM E112. Second-phase particles had a blocky and rode-like morphology, situated close to and along the grain boundaries. The secondary phase particles in this alloy are most likely included Mg-RE and Mg–Nd particles which form during solidification [42].

Fig. 5 presents an SEM image and XRD pattern of the Akermanite powder. It is clear that the range of Akermanite particle sizes were between 1 and 3 μm, particle sizes were quite similar to each other and particles had a spherical morphology. The XRD pattern of the Akermanite powder was in agreement with that of pure Akermanite standard powder (JCPDS: 01-077-1149 card), confirming the phase composition.

3.2. Microstructure of the matrix alloy after FSP

An overall OM macrograph showing the structures across different zones of the FSP WE43 sample is presented in Fig. 6 (a). This image was captured on the cross section of the sample normal to the pin-moving direction. A number of zones that are well-known in the FSP material, i.e., stir zone (SZ), thermomechanically affected zone (TMAZ), heat-affected zone (HAZ) and the base metal were all observed. To illustrate the zones, SZ was separated by a black dash line from the other zones. It can be seen that the depth of SZ was about 4 mm.

An EBSD image showing the grain structure in the SZ of the FSP WE43 alloy after six passes of FSP is presented in Fig. 6 (b). The average grain size was reduced from 18 to 2.5 μm, which indicated significant grain refinement because of dynamic recrystallization imposed by severe plastic deformation during FSP. As a result of applied deformation in the SZ zone, the density of dislocations increased. Indeed, generated heat due to friction between pin and magnesium matrix gives an opportunity to the dislocations to move and produce low angle grain boundaries. The misorientation angle of formed grain boundaries is less than 15 °, and by performing more severe plastic deformation during FSP, the misorientation angle increases, and low angle grain boundaries convert to high angle grain boundaries, and, consequently, grain refinement occurs, and new grains form [43,44]. More applied severe plastic deformation in the SZ zone leads to an increment in the density of dislocations and also intensified dynamic recovery and recrystallization. Therefore, intensified dynamic recrystallization plays a crucial role in making finer grains. In addition, higher applied severe plastic deformation due to higher flow velocity of the strain and subsequently higher dislocation density causes improvement of dynamic recovery and recrystallization and fabrication of smaller grains [34,43].

The grains were fully equiaxed, of similar sizes, and showed a random orientation distribution in the EBSD image and the inverse pole figure, all of which indicated the occurrence of dynamic recrystallization (DRX) during.

Considering the low stacking fault energy (SFE) of magnesium and the observed grain structure characteristics, these recrystallized grains

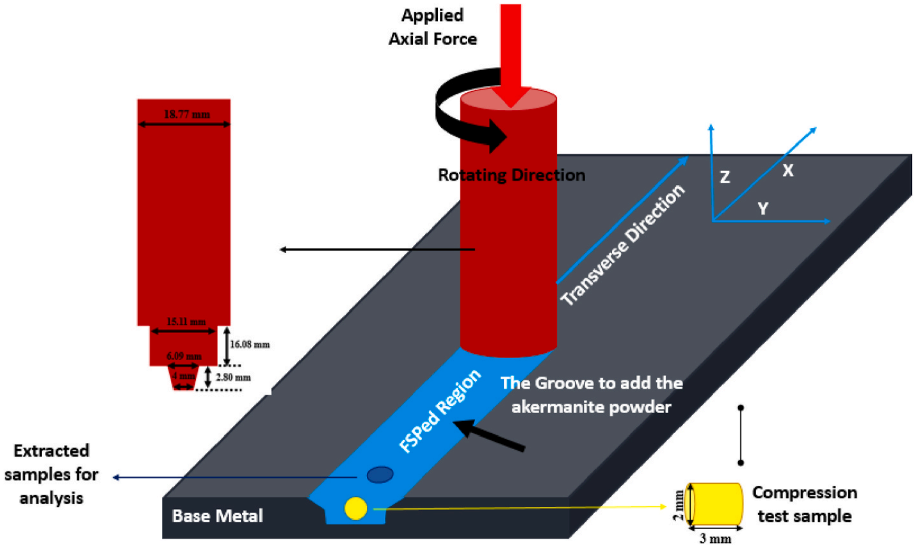

Fig. 1. Schematic illustration of FSP, the position of sample extraction and the dimensions of FSP tool.

were most likely formed through discontinuous dynamic recrystallization (DDRX) [45–48].

An SEM micrograph is given in Fig. 6 (d), showing the grain structure and second phase particles in FSP WE43 sample. By comparison with Fig. 4 showing coarser grains and many second-phase particles inside the grains and at the grain boundary regions in the as-annealed alloy, Fig. 6 clearly manifests the simultaneous occurrence of grain refinement and second-phase particle fragmentation and redistribution during FSP.

3.3. Distribution of Akermanite particles in the Mg-A composite

Fig. 7 shows the distribution of Akermanite particles in the stir zone (SZ) of WE43-A-6P sample and corresponding elemental distribution maps. It can be seen that the elements composing the Akermanite powder, i.e., Ca, Si, Mg and O, all appeared in the elemental distribution maps. In addition, many particles containing higher concentrations of Ca, Si, Mg and O, were found in these maps. These particles appeared to be agglomerated Akermanite particles. Agglomeration and clustering of Akermanite particles could occur either prior to or during FSP and might have negative influences on the mechanical properties and corrosion resistance of the composite, which could not be ascertained. Less agglomeration of Akermanite powder means a more uniform distribution on the matrix. Agglomeration may occur when particles are accumulated in some part of the SZ zone. To eliminate agglomeration of Akermanite, the powder was dispersed with ethanol and used six passes FSP to achieve better distribution. Agglomeration could lead to pores and increase inter-particles space, which could leave a negative effect on strength and corrosion resistance [33]. On the other hand, as long as the agglomerated Akermanite particles were uniformed distributed, the negative influences might not be great, as they would result in smaller interface areas between ceramic particles and the α-Mg matrix, which tended to be the preferred sites of crack initiation and corrosion attack. The presence of uniformly distributed agglomerated Akermanite particles led to the formation of a spread passive layer, which acted as effective barriers to corrosion reactions, especially localized corrosion reactions. The corrosion mechanisms will be explained in next subsections.

3.4. Corrosion resistance of the Mg-A composite

3.4.1. EIS characteristics

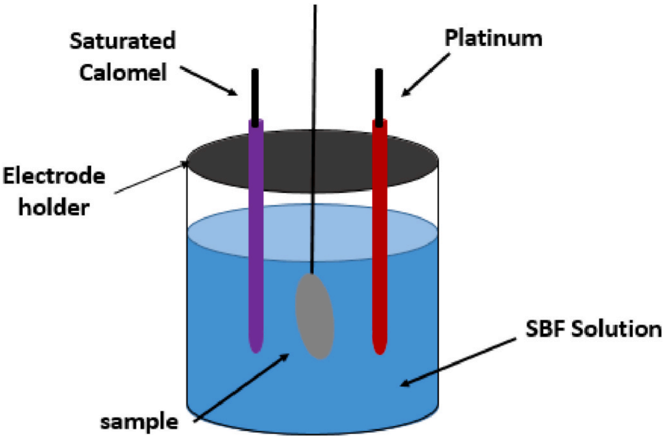

Fig. 3. The schematics of three-electrode cell used in this study for electrochemical tests.

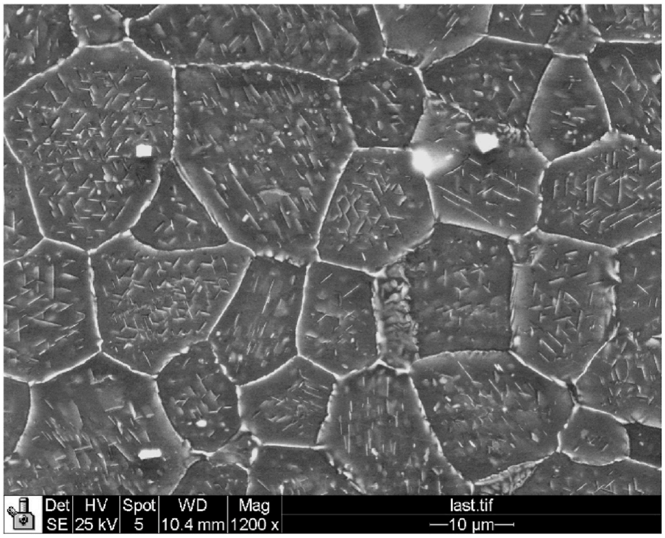

Fig. 4. Microstructure of the annealed WE43 sample prior to FSP.

Fig. 8 presents the Nyquist, bode and bode phase diagrams of WE43, WE43-6P and WE43-A-6P samples in the SBF solution. Fig. 9 shows the equivalent circuit for the samples after fitting the experimental data with the ZSimpWin 3.21 software. From the Nyquist diagrams and equivalent circuit, it is apparent that there are two capacitive loops in the high and medium frequency ranges and one inductive loop in the low frequency domain. The capacitive loops are the indicators of uniform corrosion, while the inductive loop is an indicator of absorbed species or localized pitting corrosion. The electrochemical behavior of the protective passive film and double electrical layer at the interface of WE43-SBF solution were evidenced by one capacitive loop in the Nyquist diagram. On the surface of Mg metal, as previously mentioned, firstly, a thin barrier MgO film formed. Secondly, a thick porous $Mg(OH)_2$ film formed and covered entire Mg substrate (MgO barrier film and second-phase particles). Consequently, the second-phase particles are coated with porous $Mg(OH)_2$ layer and be passive. As a consequence, the anti-corrosion properties of sample are increased. The produced Mg^{2+} cations due to dissolution of Mg at the Metal-electrolyte interface were diffused thorough porous hydroxide film. So, the high-frequency capacitive loop is related to the charge transfer resistance which involves the cathodic and anodic reactions [11] and the medium-frequency loop is correlated to double electrical layer.

Regarding to the equivalent circuit $(R_{sol}\ (Q_{dl}\ (R_t\ (L_{pitting}R_{pitting}))))$

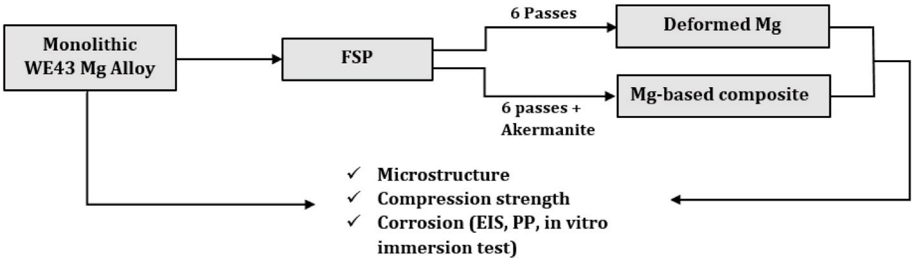

Fig. 2. the schematics of process procedure in this study.

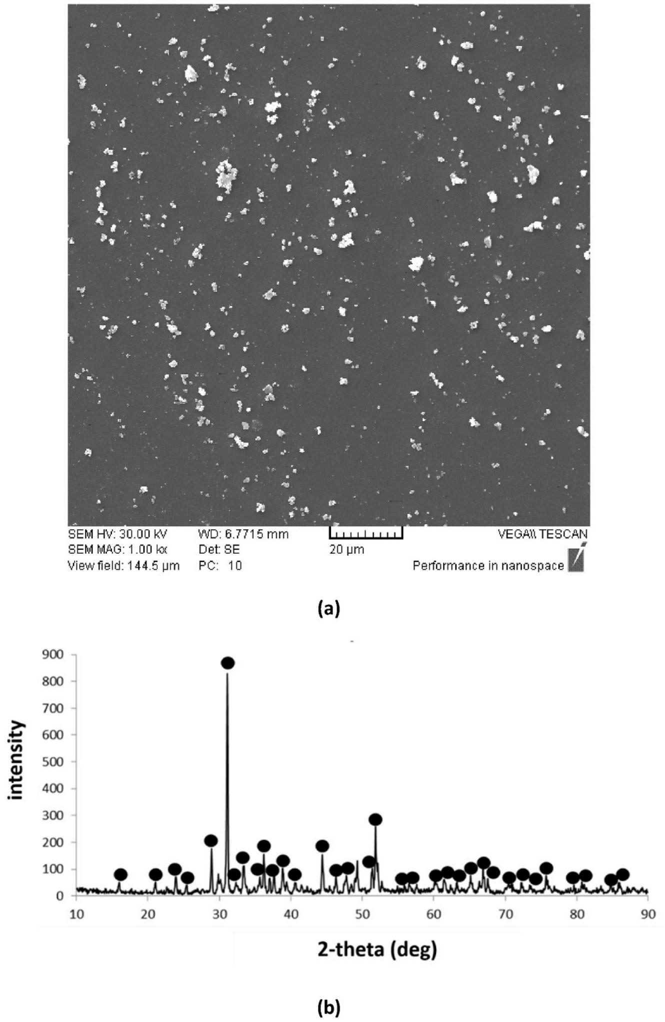

(a)

(b)

Fig. 5. (a) SEM image and (b) XRD pattern of the Akermanite powder.

(C_fR_f)) shown in Fig. 9, the corrosion mechanism was a combination of uniform corrosion and localized pitting corrosion. In the equivalent circuit, R_{sol}, C_f, R_f, Q_{dl} and R_t present the electrical resistance of the SBF solution, electrical capacitance of the protective passive films, electrical resistance of the protective passive films, phase element of the double electrical layer and charge transfer resistance of the WE43-protective passive film interface, respectively. $L_{pitting}$ and $R_{pitting}$ indicate the inductive behavior of formed pits. These electrochemical parameters were obtained from fitting experimental data and are reported in Table 2. The phase element of double electrical layer (CPE_{dl}) indicates the dielectric properties and deviation from the capacitive properties of the double electrical layer. A small amount of CPE_{dl} and a low deviation from the ideal capacitive behavior indicate a bigger capacitive loop and higher corrosion resistance with more homogenous surface. Applied FSP process and addition of Akermanite powder caused to a size increase in both high- and medium-frequency capacitive loops and also in the low frequency inductive loop, which are indicating an increase in corrosion resistance. The formed pits on the surface, due to the presence of second-phase particles, must have been the main result of pitting corrosion. With decreased pitting corrosion, because of the fragmentation and redistribution of second-phase particles, the depths of pits reduced and overall corrosion resistance improved. A more homogenous protective $MgO/Mg(OH)_2$ film on the surface could be of help in preventing intense electrochemical reactions. In short, applying FSP (leading to the fragmentation and redistribution of second-phase particles) and adding Akermanite particles to WE43 led to unstable pits with lower depths, which could easily re-passivate and get removed from the surface. Consequently, the uniformity of the protective passive layer increased, the value of CPE_{dl} and the deviation from the ideal capacitive behavior decreased, the electrochemical equilibrium between the anodic and cathodic reactions increased, the intensity of micro galvanic couples between the α-Mg matrix and second-phase particles decreased and eventually, corrosion resistance increased.

The slope of the linear part of the bode diagrams, "n", can be used as an indicator of the uniformity of the passive films ($MgO/Mg(OH)_2$) and its effect on corrosion behavior. Fig. 8 (b) shows the bode diagrams of WE43, WE43-6P and WE43-A-6P samples. It can be seen that by applying FSP and adding Akermanite particles, the value of "n" increased and approached 1. The uniformity of the passive film on WE43, WE43-6P and WE43-A-6P samples gradually increased, as evidenced by the variation trend of the "n" value ($n_{WE43} < n_{WE43\text{-}6P} < n_{WE43\text{-}A\text{-}6P}$). The uniformity of the passive film must be related to the sizes and distribution of second-phase particles. A more uniform passive film could more effectively protect the surface against destructive corrosive reaction.

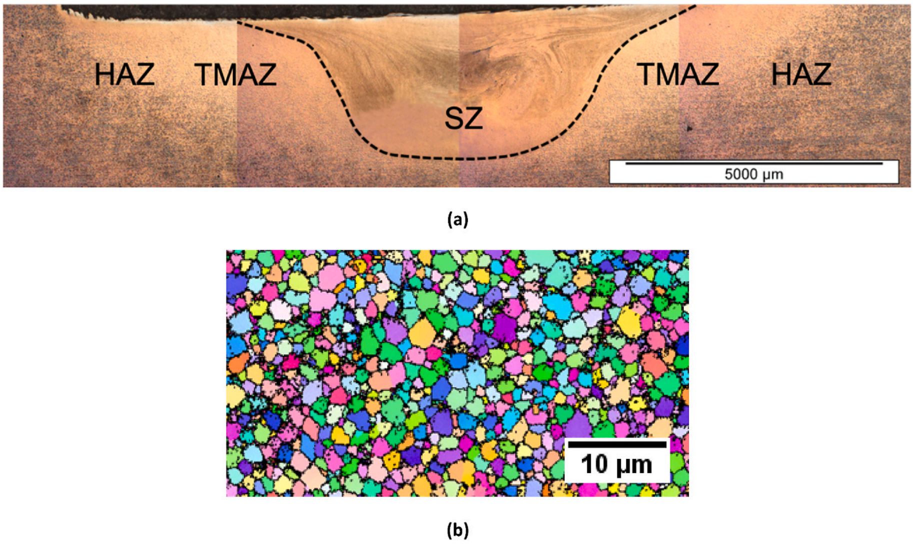

(a)

(b)

Fig. 6. (a) Multiple zones formed in the FSP WE43 alloy, (b) EBSD map showing the grain structure in the SZ of the FSP WE43 alloy, (c) inverse pole figure of the SZ of the FSP WE43 alloy, (d) low and (e) high magnification micrographs showing second-phase particles in the FSP WE43 alloy.

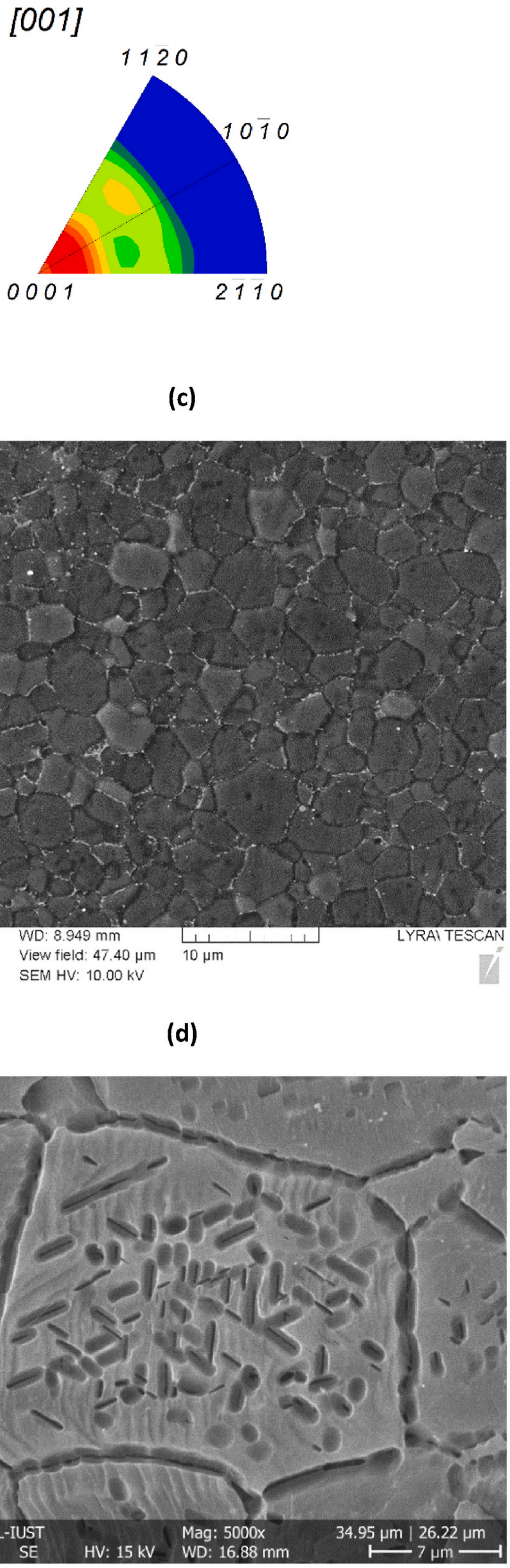

(c)

(d)

(e)

Fig. 6. (*continued*).

The bode phase diagram provides additional information about the corrosion behavior. The height of the single capacitive peak of the bode phase diagram, "h", can be used to analyze the corrosion behavior. Fig. 8 (c) shows the bode phase diagrams of WE43, WE43-6P and WE43-A-6P samples with the marked "h" parameter. The "h" parameter indicates the roughness of the surface of the sample and its influence in proceeding corrosion reactions [11,38,49]. The "h" values of WE43, WE43-6P and WE43-A-6P samples were 32.64, 26.34 and 20.81°, respectively. It is

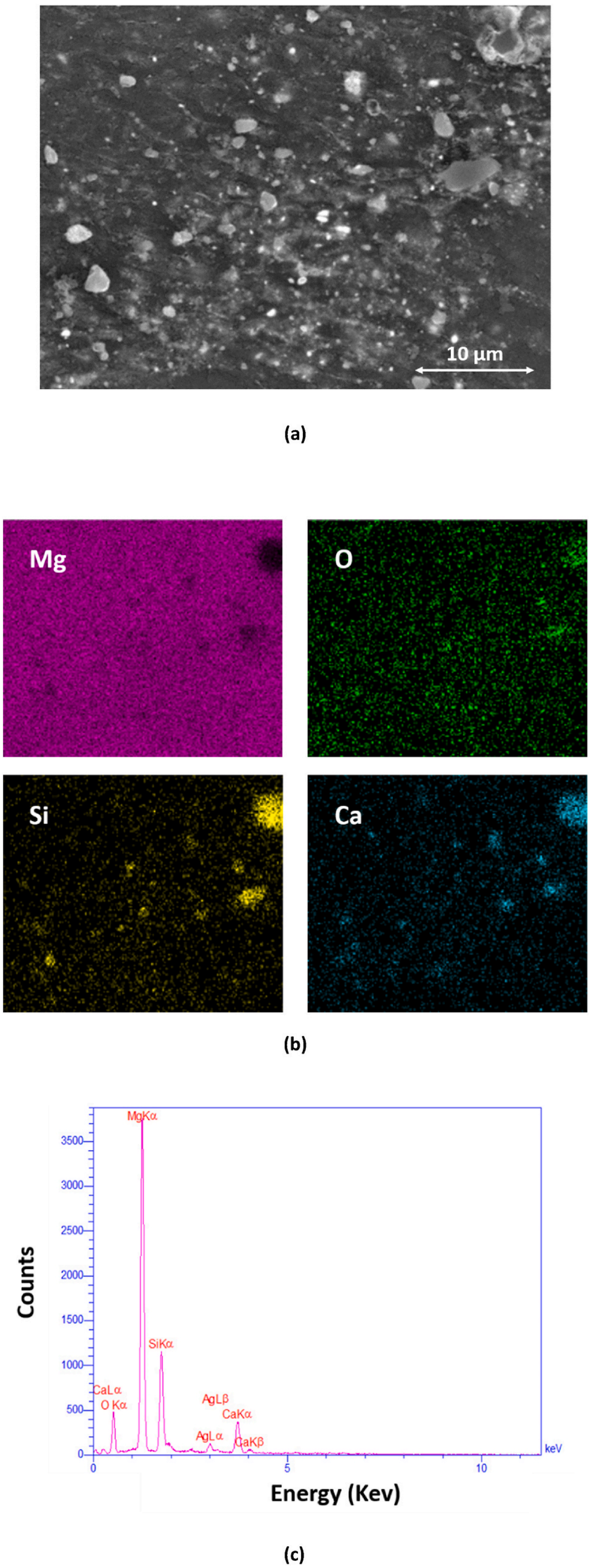

Fig. 7. (a) Distribution of Akermanite particles in the WE43 alloy (top view), (b) corresponding elemental distribution maps and (c) an EDS spectrum of Akermanite particles in the WE43 matrix.

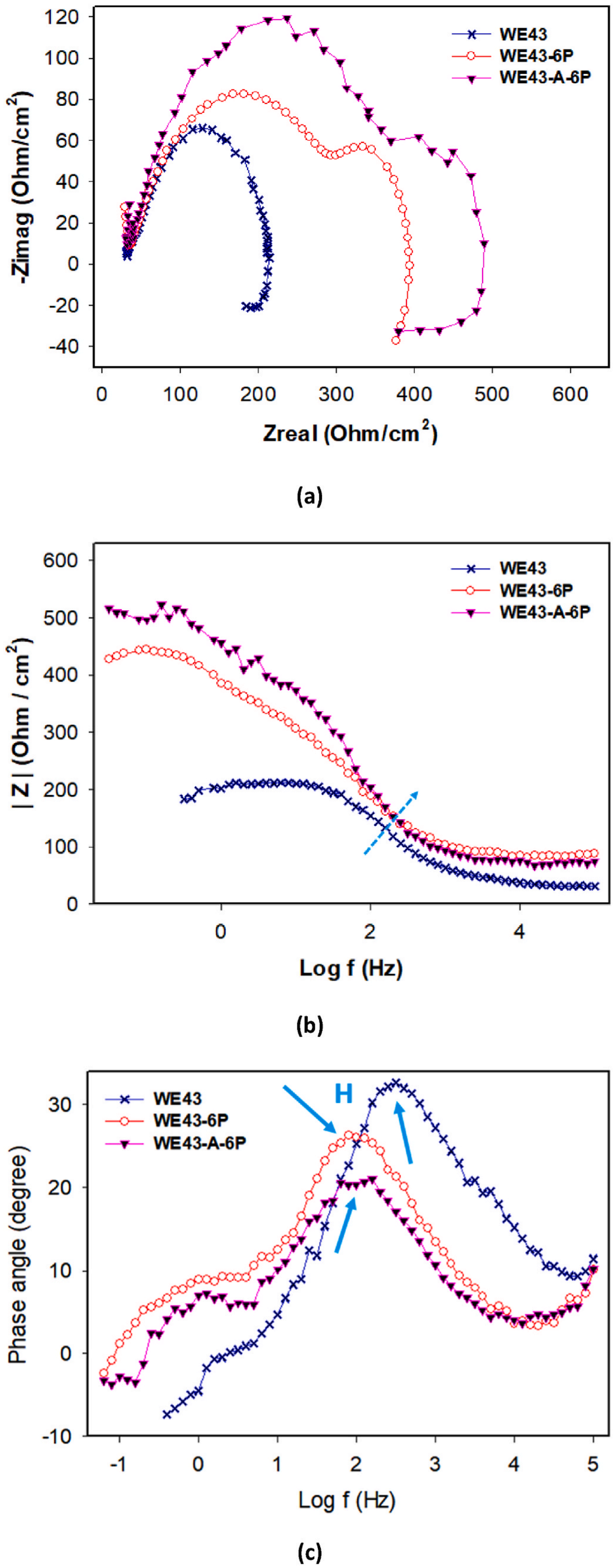

Fig. 8. (a) Nyquist, (b) bode and (c) bode phase plots of WE43, WE43-6P and WE43-A-6P samples.

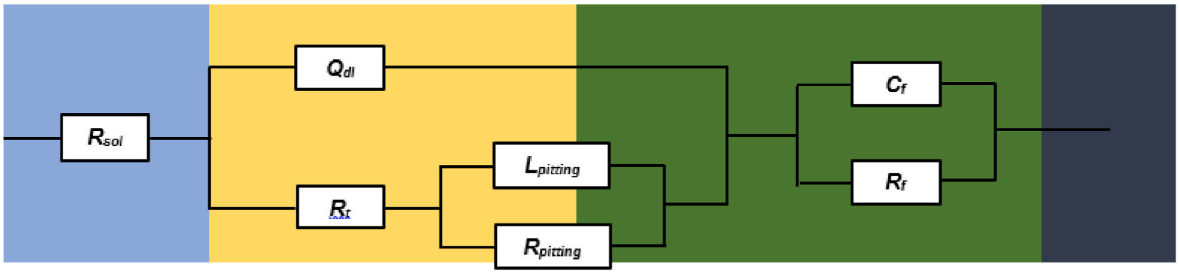

Fig. 9. Equivalent circuit diagram from EIS data fitting using the ZsimpWin 3.21 software.

Table 2
Electrochemical parameters calculated from the experimental EIS data.

Sample	R_{sol} (Ohm/cm^2)	(Q-m)$_{dl}$	R_{dl} (Ohm/cm^2)	R_{pit} (Ohm/cm^2)	L_{pit} (H/cm^2)	K_{square}
WE43	24.85	0.891	283.25	21.17	141.15	5.18×10^{-5}
WE43-6P	24.72	0.745	364.11	36.85	233.42	2.58×10^{-5}
WE43-A-6P	24.36	0.713	402.98	42.03	345.62	1.94×10^{-5}

Table 3
Electrochemical parameters from potentiodynamic polarization analysis.

sample	I_{Corr} (μA/cm^2)	E_{Corr} (V vs SCE)	**β_a** (mV.dec^{-1})	-**β_c** (mV.dec^{-1})	**R_P** (kΩ/cm^2)	mpy (mm/year)
WE43	206.161	−1.602	160.413	211.37	0.192	4.613
WE43-6P	141.496	−1.536	172.375	306.787	0.339	3.166
WE43-A-6P	62.2	−1.535	147.288	214.504	0.609	1.391

clear that by applying FSP and adding Akermanite particles to WE43, the roughness of surface increased and consequently the corrosion resistance improved. Therefore, the WE43-A-6P sample with the highest values of "n" and "h" showed the highest corrosion resistance.

3.4.2. Potentiodynamic polarization behavior

Fig. 10 shows the potentiodynamic polarization diagrams of WE43, WE43-6P and WE43-A-6P samples. The electrochemical parameters from polarization curves, i.e., I_{corr}, E_{corr}, β_a (the slope of anodic branch) and β_c (the slope of cathodic branch), mpy and R_p, were calculated with the Versa STAT 4 software by drawing tangent lines on the anodic and cathodic branches. The values are given in Table 3. The mpy value indicating the weight loss per year as an indicator of corrosion rate in the SBF solution, was calculated using Eq. (1) [50]:

$$\text{mpy} = \frac{0.00327 \times i_{corr} \times (\text{E.W})}{n \times \rho} \tag{1}$$

where n is the number of exchanged electrons in the dissolution reaction (+2 for Mg), ρ is the density of the WE43 alloy, and E.W is the equivalent weight of the WE43 alloy. In addition, R_p represents the polarization resistance of the sample and can be calculated using Eq. (2) [50]:

$$R_p = \frac{1}{2.303\left(\frac{1}{\beta_a} + \frac{1}{\beta_c}\right) i_{corr}} \tag{2}$$

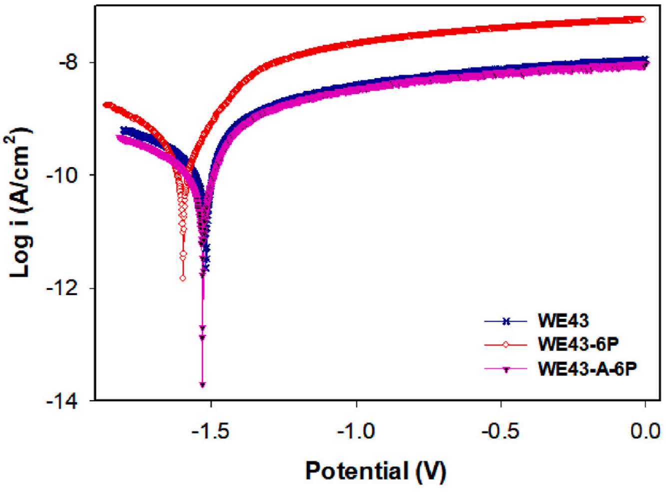

Fig. 10. Potentiodynamic polarization diagrams of WE43, WE43-6P and WE43-A-6P samples.

It can be seen in Table 3 that the I_{corr} and mpy values decreased from 206.161 μA/cm^2 and 4.613 mm/year to 141.496 μA/cm^2 and 3.166 mm/year, respectively, while the R_p value increased from 0.192 to 0.339 Ω/cm^2, as a result of FSP. As severe plastic deformation during FSP led to the fragmentation and redistribution of second-phase particles and grain refinement, a uniform distribution of particles was achieved in the WE43 alloy, causing diminished intensity of micro galvanic couples and resulting in more uniform corrosion reactions. Because of an increase in number density and a decrease in the sizes of second-phase particles, the E_{corr} value reduced to a more negative value (−1.536 V) and the activation energy of corrosion reactions would thus be reduced (i.e., thermodynamic aspect of corrosion).

As a result, the number density of pits increased and their sizes decreased. The formed pits became unstable, which might re-passivate and get removed from the surface of the substrate. Moreover, according to literatures, two different passive films could form on the Mg surface. The first one is the thin barrier MgO film on the surface of metal that could not cover the intermetallic particles. The second one is the thick porous $Mg(OH)_2$ film that form on top of the barrier film and intermetallic particles [11,51,52]. The dissolved Mg^{2+} ions at the interface diffuse through $Mg(OH)_2$ porous film. The formation of the passive films (MgO or $Mg(OH)_2$) in the fine-grained structure is known to be faster and able to prevent further destruction of the surface [17,23,38,39,53]. Once the WE43 alloy is brought to contact with an electrolyte, a protective passive film forms through an anodic reaction which is related to the dissolution of magnesium ions at the interface of Mg surface-SBF electrolyte according to Eq. (4):

$$2H^+ + 2e^- = H_2 \text{ (cathodic reaction)} \tag{3}$$

$$Mg = Mg^{2+} + 2e^- \text{ (anodic reaction)} \tag{4}$$

Then, first MgO and after $Mg(OH)_2$ films form on the surface, according to Eqs. (5) and (6) [11,54,55]:

$$Mg + O = MgO \tag{5}$$

$$Mg^{2+} + 2OH^- = Mg(OH)_2 \tag{6}$$

The interactions between the above-mentioned factors led to an increase in the polarization resistance. Furthermore, due to the addition of Akermanite to the WE43 alloy and the formation of a surface composite, the I_{corr} and mpy values decreased from 141.496 μA/cm^2 and 3.166 mm/year to 62.2 μA/cm^2 and 1.391 mm/year, respectively. In addition, the R_p value increased from 0.339 to 0.609 Ω/cm^2. It was found that the presence of Akermanite particles at the surface of WE43 indeed improved the corrosion resistance. Calcium silicate-based ceramics including Akermanite are biodegradable in SBF but more corrosion resistant than magnesium. Therefore, a uniform distribution of Akermanite particles on the surface could result in further improved corrosion resistance.

Fig. 11 shows the corroded surfaces of WE43, WE43-6P and WE43-A-6P samples after the potentiodynamic polarization tests. It is clear that the uniformity of corroded surface increased from WE43 to WE43-6P and to WE43-A-6P samples and the intensity of corrosion attacks reduced. Akermanite particles had strong structural bonding with the matrix, acted as obstacles to corrosion reactions, and reduced the formation of stable pitting. In summary, the WE43-A-6P composite showed the best polarization resistance with the highly uniformed corroded surface.

3.4.3. In vitro degradation behavior during immersion in SBF

The corrosion reactions and generation of pits both have thermodynamic and kinetics aspects. E_{corr} shows the thermodynamic aspect indicating the required driving force for proceeding corrosion reactions, while I_{corr} represents the kinetic aspect of corrosion in controlled polarization test. In vitro immersion test is used for investigating the kinetic aspect of corrosion reactions without applying any potential or current. The variations of mass loss rate and pH with immersion time in SBF solution at 37 °C are shown in Fig. 12. The variation of mass loss rate is directly related to the corrosion rate of the sample and the formation of a natural protective film on the surface. The values of mass loss rate were calculated by Eq. (7) [50],:

$$R = \frac{km}{A\rho t} \tag{7}$$

where:

CR = Mass loss rate
k = Constant (8.76×10^4)
m = Mass loss (g).
A = Exposed area (cm^2).
ρ = Density of the WE43 alloy (g/cm^3).
t = Immersion time (h).

It is clear that during immersion, the rate of mass loss by passing time

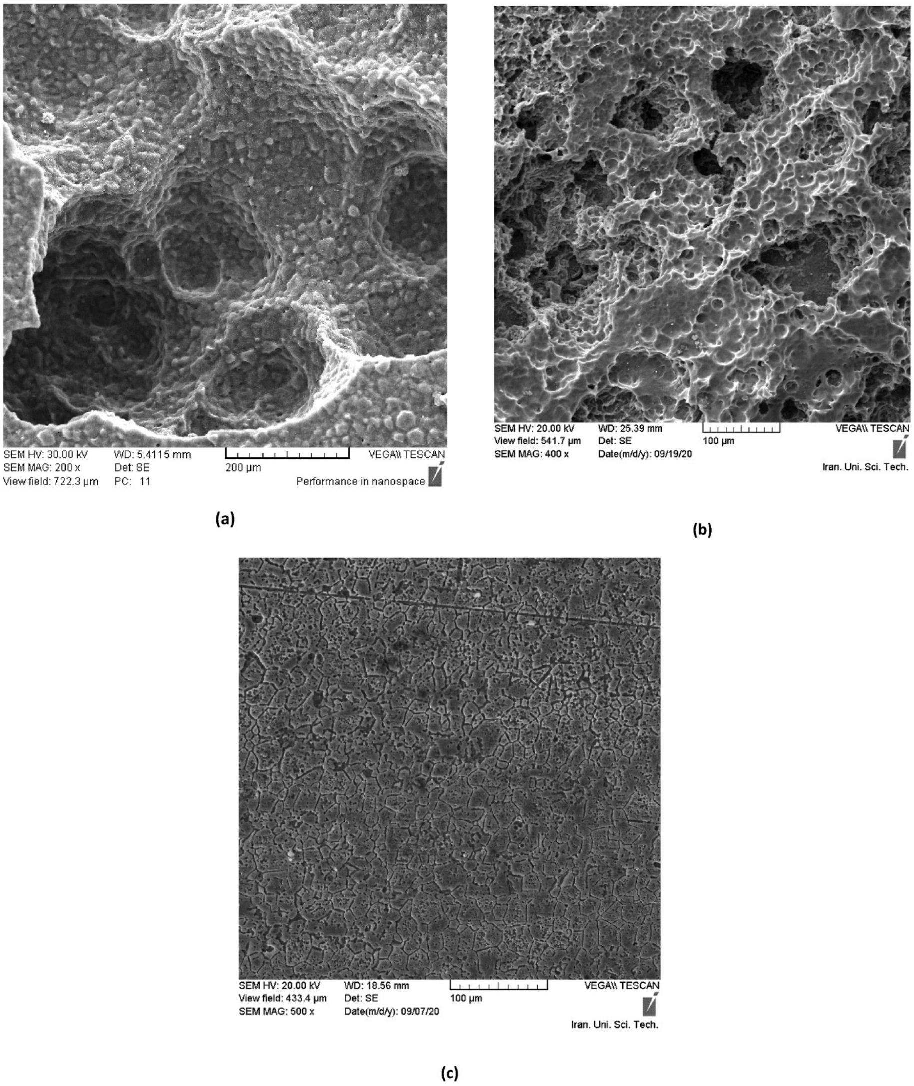

(a)

(b)

(c)

Fig. 11. SEM images showing the surfaces of (a) WE43, (b) WE43-6P and (c) WE43-A-6P samples after potentiodynamic polarization in the SBF solution.

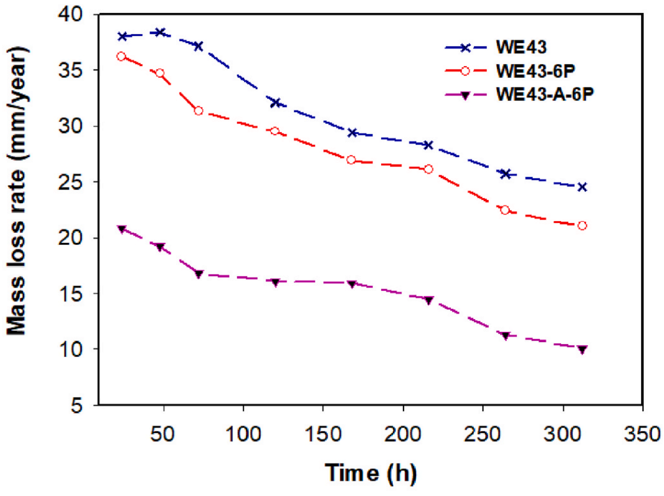

(a)

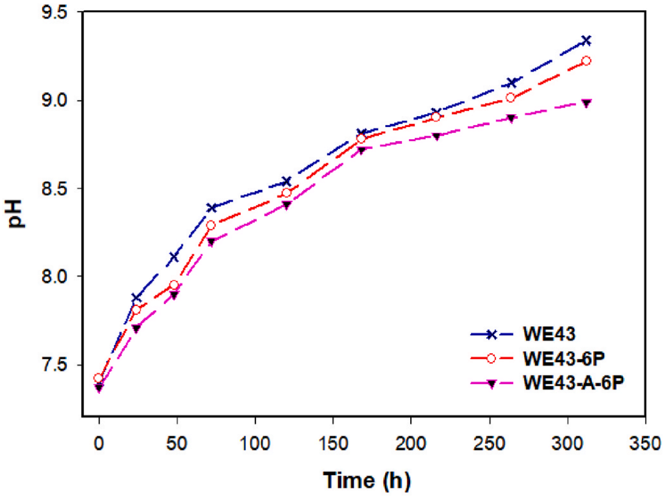

(b)

Fig. 12. Variations of (a) mass loss rate of WE43, WE43-6P and WE43-A-6P samples and (b) the value of pH with increasing immersion time.

was decreased because of the formation of the passive film and its protective effect. By increasing immersion time, the compactness of passive film increased and became more impenetrable. Therefore, exposure of WE43 surface with corrosive ions in SBF solution decreased, and passive film could be more effective in the protection mechanism. As a result, the mass loss rate of samples with increasing immersion time was reduced. Moreover, the mass loss rate of the fabricated composite sample with Akermanite powder is less than the as-received WE43 sample. This is because of grain refinement and the uniform structure of fragmented second-phase particles, which leads to the formation of compacter and more uniform passive films.

It is observable that by increasing immersion time, the concentration of H^+ reduced, and the value of pH increased. In fact, the H^+ cations reacted with Mg^{2+} cations and $MgO/Mg(OH)_2$ layer as the passive film created on the surface. By passing time, the reaction between H^+ and Mg^{2+} cations increased, and the $MgO/Mg(OH)_2$ passive film became compacter and thicker. By consuming H^+ cations in reactions with Mg^{2+}, the value of pH increased. The overall weight of samples in each immersion time is an evaluation of reduction of weight because of dissolution of Mg and increment of weight because of formation of $MgO/Mg\ (OH)_2$ passive film.

It can be seen that there are the same variations of corrosion results of different samples in potentiodynamic polarization, EIS and immersion tests. In summary, the WE43-A-6P composite exhibited the highest corrosion resistance and the WE43 sample prior to FSP had the poorest corrosion resistance.

3.5. Mechanical properties of the Mg-A composite

Fig. 13 shows the stress-strain curves obtained from the uniaxial compression tests of monolithic WE43 alloy, WE43-6P and WE43-A-6P composite specimens. It is clear that the compressive strength and ductility (i.e., strain to failure e_f) values of WE43-6P and WE43-A-6P specimens were much higher than those of the WE43 alloy without experiencing FSP. The improvements in compressive strength and ductility could be attributed to the reductions in grain size and fragmentation and redistribution of second-phase particles as a result of severe plastic deformation involved in FSP. As grain size reduced, the density of grain boundaries increased. Grain boundaries and fragmented second-phase particles can act as obstacles in the movement route of dislocations and lead to improvement of strength. Volume fraction, distribution, size, and shape of second-phase particles (or additive particles like Akermanite) and interparticle distances between particles are effective parameters in strengthening mechanisms by particles. So, by achieving uniform and fragmented second-phase particles during FSP, the strengthening effect is improved [14,15].

As shown earlier in Fig. 4, second-phase particles in WE43 sample were located continuously along the grain boundaries, which could have a negative effect on the mechanical properties of the WE43 alloy. The occurrence of fragmentation and redistribution of second-phase particles during FSP indeed led to beneficial effects on the mechanical properties. These results are in agreement with those reported by other researchers who found that grain reinforcement and second-particle fragmentation and redistribution could lead to improved mechanical properties and corrosion resistance of magnesium alloys [38,56–61].

The ultimate compressive strength (UCS) and yield strength (YS) values of WE43, WE43-6P and WE43-A-6P specimens are reported in Fig. 14. As a result of the reinforcing effect of Akermanite particles on the α-Mg matrix, the WE43-A-6P specimen exhibited the highest UCS and YS, in comparison to WE43 and WE43-6P specimens. In addition, the value of e_f(%) for WE43, WE43-6P and WE43-A-6P samples are 4.5, 16 and 22, respectively. It can be concluded that the ductility of WE43-A-6P specimen was markedly enhanced, which was quite unusual for metal-matrix composites whose ductility is typically compromised by the presence of embedded ceramic particles [62]. This remarkable improvement could be attributed to the significant reduction in grain

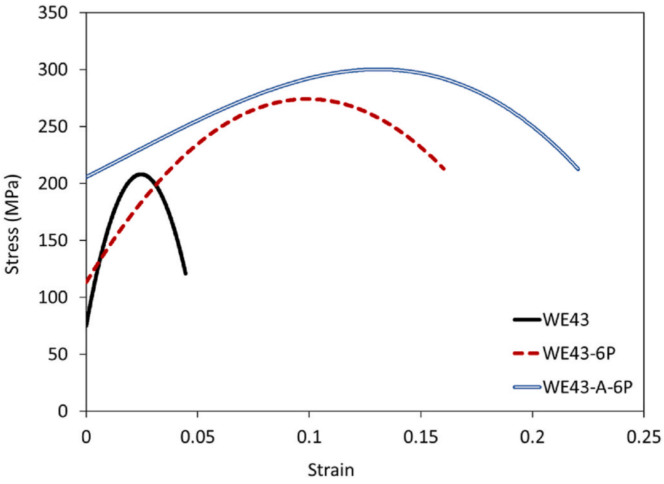

Fig. 13. Stress-strain curves obtained from uniaxial compression tests.

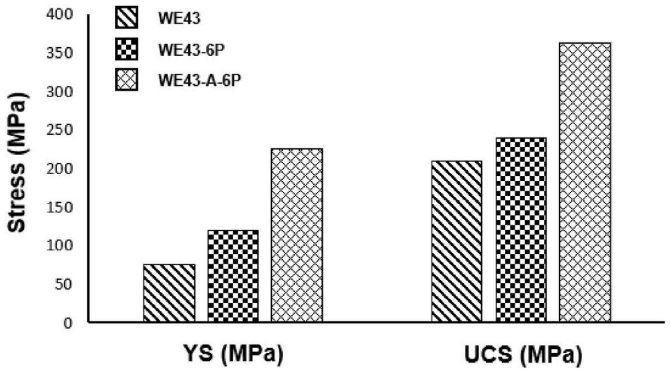

Fig. 14. The values of ultimate compressive strength (UCS) and yield strength (YS) of WE43, WE43-6P and WE43-A-6P samples.

size and fragmentation and redistribution of second-phase particles, which were continuously distributed along the grain boundaries in the as-annealed state (prior to FSP). Indeed, by grain refinement during FSP, the fracture mechanism is converted from intergranular fracture to transgranular fracture [63,64]. Grain boundaries, besides inhibition of dislocation movement, can be effective in reducing crack growth and consequently improving ductility [43,44]. During FSP, by applying cumulative strains and raising local temperature, grains became refined through dynamic recrystallization (DRX). In the WE43 magnesium alloy, the DRX mechanism most likely includes discontinuous DRX via nucleation and growth [65,66]. It should be mentioned that temperature rise during FSP could cause grain growth directly after DRX. However, second-phase particles and ceramic particles in the composite could exert a pinning effect against grain growth.

Magnesium has an elastic modulus of 42 GPa, which is close to that of human bone and consequently this can largely overcome the drawback of other metallic implant materials with much higher Young's modulus, which may cause stress shielding [67–69]. However, magnesium suffers from low strength, even compared to human thigh bones, which consequently limits its applications to repairing or regenerating no or low load-bearing bones. For load-bearing applications, sufficient strength is needed right after implantation and a certain strength must be retained throughout the biodegradation period, e.g., three months. It can be seen in Fig. 14 that the UCS of the as-annealed monolithic WE43 alloy is 210 MPa, which is higher than the strengths of human thigh bones ranging from 130 to 205 MPa [70–73], but only marginally higher than the strength of human femur in a healthy body. As a matter of fact, the as-annealed monolithic WE43 alloy with a YS value of 75 MPa is not really suitable for load-bearing implant applications, because the minimum strength of an implant after implantation must be at least equal to the strength of human bone. An easy solution might be to increase the cross-sectional area of the implant so as to provide required load-bearing capability. Apart from the fact that such a solution might be anatomically not desirable or feasible, an increase in cross section may result in an increased stress-shielding effect due to an increase in the stiffness of the implant. Therefore, increasing the cross-sectional area of the implant does not seem to be the right approach to compensating for the low strength of magnesium. Moreover, a biodegradable implant becomes weaker over time along with its biodegradation. In other words, further improvements of the WE43 magnesium alloy in mechanical properties are very much desired, although it is already advantageous when compared to biodegradable polymers [74,75]. It can be seen in Fig. 14 that when this alloy is processed by FSP, even without ceramic particle reinforcement, it may marginally meet the minimum requirements for a load-bearing implant material. With the addition of ceramic particles, the composite can attain a yield strength, which is 3 times as high as the YS of the as-annealed WE43 alloy, thereby leaving a certain strength margin for strength reduction during its biodegradation. Actually, such an improvement in compressive strength is necessary, as other researchers have already shown that the biodegradation rate may significantly increase, when the implant is subjected to physiological loading [6,12,25]. In addition, the fluidity of the electrolyte in vivo also affects the biodegradation rate of Mg-based materials by introducing shear stresses and affecting the adhesion of corrosion products to the substrate and local pH [76]. In addition, simultaneous actions of stress and corrosion may result in the activation of stress corrosion cracking (SCC) [77–82] or corrosion fatigue [79,83–86]. Mechanical stability during the healing and recovery of damaged bone is a basic requirement of an implant for orthopedic treatments, which is based on sufficient mechanical strength and strength retention during biodegradation [76,87]. The achieved improvements in strength and ductility through FSP and ceramic particle reinforcement in this research could offer the required mechanical stability. Thus, the FSP composite could become a candidate material for load-bearing orthopedic applications.

4. Conclusions

The research was intended to confirm the hypothesis that the combination of applying FSP and adding Akermanite ceramic particles to the WE43 alloy would result in improved mechanical properties and corrosion resistance. The main results are listed below:

1. By applying FSP to the alloy up to six passes, second-phase particles became fragmented and redistributed in the α-Mg matrix, and the grain structure was significantly refined to an average size of 2.5 μm. Also, the uniformity of additive Akermanite powder is improved.
2. The composite showed the highest strength and the highest ductility.
3. The corrosion mechanism of the materials was a combination of uniform and localized pitting corrosion. The improvement in corrosion resistance after applying FSP and adding Akermanite particles was attributed to more uniform corrosion and reduced pitting corrosion.
4. The uniformity of the corroded surface is improved by applying six passes FSP and the addition of Akermanite powder.
5. Applying six passes FSP causes to form a more uniform, stable, and compact passive film on deformed composite. Therefore, corrosion resistance significantly increased.
6. Regarding immersion test, the value of pH of electrolyte and mass loss of samples is increased, and the concentration of H^+ cations and corrosion rate is decreased by increasing immersion time. At the same time, the corrosion rate and mass loss of WE43-A-6P are higher than other samples.

CRediT authorship contribution statement

M. Mehdizade: Software, Data curation, Writing – original draft. **A. R. Eivani:** Conceptualization, Supervision. **F. Tabatabaei:** Methodology, Investigation, Data curation. **H.R. Jafarian:** Project administration. **J. Zhou:** Conceptualization.

Declaration of Competing interest

The authors declare that they have no known competing financial interests or personal relationships that could have appeared to influence the work reported in this paper.

Data availability

Data will be made available on request.

References

[1] I. Johnson, H. Liu, A study on factors affecting the degradation of magnesium and a magnesium-yttrium alloy for biomedical applications, PLoS One 8 (2013), https://doi.org/10.1371/journal.pone.0065603.

[2] L. Liu, K. Gebresellasie, B. Collins, H. Zhang, Z. Xu, J. Sankar, Y.C. Lee, Y. Yun, Degradation rates of pure zinc, magnesium, and magnesium alloys measured by volume loss, mass loss, and hydrogen evolution, Appl. Sci. 8 (2018), https://doi.org/10.3390/app8091459.

[3] B.R. Sunil, A.A. Kumar, T.S. Sampath Kumar, U. Chakkingal, Role of biomineralization on the degradation of fine grained AZ31 magnesium alloy processed by groove pressing, Mater. Sci. Eng. C 33 (2013) 1607–1615, https://doi.org/10.1016/j.msec.2012.12.095.

[4] M.P. Staiger, A.M. Pietak, J. Huadmai, G. Dias, Magnesium and its alloys as orthopedic biomaterials: a review, Biomaterials 27 (2006) 1728–1734, https://doi.org/10.1016/j.biomaterials.2005.10.003.

[5] F. Witte, The history of biodegradable magnesium implants: a review, Acta Biomater. 6 (2010) 1680–1692, https://doi.org/10.1016/j.actbio.2010.02.028.

[6] F. Witte, N. Hort, C. Vogt, S. Cohen, K.U. Kainer, R. Willumeit, F. Feyerabend, Degradable biomaterials based on magnesium corrosion, Curr. Opin. Solid State Mater. Sci. 12 (2008) 63–72, https://doi.org/10.1016/j.cossms.2009.04.001.

[7] M. Pogorielov, E. Husak, A. Solodivnik, S. Zhdanov, Magnesium-based biodegradable alloys: degradation, application, and alloying elements, Interv. Med. Appl. Sci. 9 (2017) 27–38, https://doi.org/10.1556/1646.9.2017.1.04.

[8] L. Li, J. Gao, Y. Wang, Evaluation of cyto-toxicity and corrosion behavior of alkali-heat-treated magnesium in simulated body fluid, Surf. Coating. Technol. 185 (2004) 92–98, https://doi.org/10.1016/j.surfcoat.2004.01.004.

[9] J. Wang, Y. He, M.F. Maitz, B. Collins, K. Xiong, L. Guo, Y. Yun, G. Wan, N. Huang, A surface-eroding poly(1,3-trimethylene carbonate) coating for fully biodegradable magnesium-based stent applications: toward better biofunction, biodegradation and biocompatibility, Acta Biomater. 9 (2013) 8678–8689, https://doi.org/10.1016/j.actbio.2013.02.041.

[10] N.T. Kirkland, N. Birbilis, M.P. Staiger, Assessing the corrosion of biodegradable magnesium implants: a critical review of current methodologies and their limitations, Acta Biomater. 8 (2012) 925–936, https://doi.org/10.1016/j.actbio.2011.11.014.

[11] G. Baril, G. Galicia, C. Deslouis, N. Pébère, B. Tribollet, V. Vivier, An impedance investigation of the mechanism of pure magnesium corrosion in sodium sulfate solutions, J. Electrochem. Soc. 154 (2007) C108, https://doi.org/10.1149/1.2401056.

[12] N. Hort, Y. Huang, D. Fechner, M. Störmer, C. Blawert, F. Witte, C. Vogt, H. Drücker, R. Willumeit, K.U. Kainer, F. Feyerabend, Magnesium alloys as implant materials-Principles of property design for Mg-RE alloys, Acta Biomater. 6 (2010) 1714–1725, https://doi.org/10.1016/j.actbio.2009.09.010.

[13] Q. Liu, G. qiang Chen, S. bo Zeng, S. Zhang, F. Long, Q. yu Shi, The corrosion behavior of Mg-9Al-xRE magnesium alloys modified by friction stir processing, J. Alloys Compd. 851 (2021), 156835, https://doi.org/10.1016/j.jallcom.2020.156835.

[14] B. Bagheri, M. Abbasi, A. Abdollahzadeh, S.E. Mirsalehi, Effect of second-phase particle size and presence of vibration on AZ91/SiC surface composite layer produced by FSP, Trans. Nonferrous Met. Soc. China (English Ed. 30 (2020) 905–916, https://doi.org/10.1016/S1003-6326(20)65264-5.

[15] A. Abdollahzadeh, B. Bagheri, M. Abbasi, F. Sharifi, A. Ostovari Moghaddam, Mechanical, wear and corrosion behaviors of AZ91/SiC composite layer fabricated by friction stir vibration processing, Surf. Topogr. Metrol. Prop. 9 (2021), https://doi.org/10.1088/2051-672X/ac2176.

[16] O. Esmaeilzadeh, A.R. Eivani, M. Mehdizade, S.M.A. Boutorabi, S. M. Masoudpanah, An investigation of microstructural background for improved corrosion resistance of WE43 magnesium-based composites with ZnO and Cu/ZnO additions, J. Alloys Compd. 908 (2022), 164437, https://doi.org/10.1016/j.jallcom.2022.164437.

[17] A.R. Eivani, F. Tabatabaei, A.R. Khavandi, M. Tajabadi, M. Mehdizade, H. R. Jafarian, J. Zhou, The effect of addition of hardystonite on the strength, ductility and corrosion resistance of WE43 magnesium alloy, J. Mater. Res. Technol. 13 (2021) 1855–1865, https://doi.org/10.1016/j.jmrt.2021.05.027.

[18] S. Jaiswal, R.M. Kumar, P. Gupta, M. Kumaraswamy, P. Roy, D. Lahiri, Mechanical, corrosion and biocompatibility behaviour of Mg-3Zn-HA biodegradable composites for orthopaedic fixture accessories, J. Mech. Behav. Biomed. Mater. 78 (2018) 442–454, https://doi.org/10.1016/j.jmbbm.2017.11.030.

[19] B. Ratna Sunil, T.S. Sampath Kumar, U. Chakkingal, V. Nandakumar, M. Doble, Friction stir processing of magnesium-nanohydroxyapatite composites with controlled in vitro degradation behavior, Mater. Sci. Eng. C 39 (2014) 315–324, https://doi.org/10.1016/j.msec.2014.03.004.

[20] P. Srinath, P. Abdul Azeem, K. Venugopal Reddy, Review on calcium silicate-based bioceramics in bone tissue engineering, Int. J. Appl. Ceram. Technol. 17 (2020) 2450–2464, https://doi.org/10.1111/ijac.13577.

[21] M. Diba, O.M. Goudouri, F. Tapia, A.R. Boccaccini, Magnesium-containing bioactive polycrystalline silicate-based ceramics and glass-ceramics for biomedical applications, Curr. Opin. Solid State Mater. Sci. 18 (2014) 147–167, https://doi.org/10.1016/j.cossms.2014.02.004.

[22] C. Wu, J. Chang, A novel akermanite bioceramic: preparation and characteristics, J. Biomater. Appl. 21 (2006) 119–129, https://doi.org/10.1177/0885328206057953.

[23] A.R. Eivani, M. Mehdizade, S. Chabok, J. Zhou, Applying multi-pass friction stir processing to refine the microstructure and enhance the strength, ductility and corrosion resistance of WE43 magnesium alloy, J. Mater. Res. Technol. 12 (2021) 1946–1957, https://doi.org/10.1016/j.jmrt.2021.03.021.

[24] N. Kumar, R.S. Mishra, N.B. Dahotre, R.E. Brennan, K.J. Doherty, K.C. Cho, Effect of friction stir processing on microstructure and mechanical properties of laser-processed [Formula presented] alloy, Mater. Des. 110 (2016) 663–675, https://doi.org/10.1016/j.matdes.2016.08.039.

[25] F. Liu, Y. Ji, Z. Sun, J. Liu, Y. Bai, Z. Shen, Enhancing corrosion resistance and mechanical properties of AZ31 magnesium alloy by friction stir processing with the same speed ratio, J. Alloys Compd. 829 (2020), 154452, https://doi.org/10.1016/j.jallcom.2020.154452.

[26] B.R. Sunil, G.P.K. Reddy, H. Patle, R. Dumpala, Magnesium based surface metal matrix composites by friction stir processing, J. Magnes. Alloy. 4 (2016) 52–61, https://doi.org/10.1016/j.jma.2016.02.001.

[27] G. Cao, D. Zhang, W. Zhang, W. Zhang, In vitro corrosion study of friction stir processed WE43 magnesium alloy in a simulated body fluid, Materials 9 (2016), https://doi.org/10.3390/ma9070542.

[28] H. Seifiyan, M. Heydarzadeh Sohi, M. Ansari, D. Ahmadkhaniha, M. Saremi, Influence of friction stir processing conditions on corrosion behavior of AZ31B magnesium alloy, J. Magnes. Alloy. 7 (2019) 605–616, https://doi.org/10.1016/j.jma.2019.11.004.

[29] X.C. Luo, L.M. Kang, H.L. Liu, Z.J. Li, Y.F. Liu, D.T. Zhang, D.L. Chen, Enhancing mechanical properties of AZ61 magnesium alloy via friction stir processing: effect of processing parameters, Mater. Sci. Eng. 797 (2020), https://doi.org/10.1016/j.msea.2020.139945.

[30] R.S. Mishra, Z.Y. Ma, Friction stir welding and processing, Mater. Sci. Eng. R Rep. 50 (2005) 1–78, https://doi.org/10.1016/j.mser.2005.07.001.

[31] M.M. El-Sayed, A.Y. Shash, M. Abd-Rabou, M.G. ElSherbiny, Welding and processing of metallic materials by using friction stir technique: a review, J. Adv. Join. Process. 3 (2021), 100059, https://doi.org/10.1016/j.jajp.2021.100059.

[32] D. Rahmatabadi, M. Ahmadi, M. Pahlavani, R. Hashemi, DIC-based experimental study of fracture toughness through R-curve tests in a multi-layered Al-Mg (LZ91) composite fabricated by ARB, J. Alloys Compd. 883 (2021), 160843, https://doi.org/10.1016/j.jallcom.2021.160843.

[33] B. Bagheri, A. Abdollahzadeh, F. Sharifi, M. Abbasi, The role of vibration and pass number on microstructure and mechanical properties of AZ91/SiC composite layer during friction stir processing, Proc. Inst. Mech. Eng. Part C J. Mech. Eng. Sci. 236 (2022) 2312–2326, https://doi.org/10.1177/09544062211024281.

[34] M. Abbasi, B. Bagheri, F. Sharifi, Simulation and experimental study of dynamic recrystallization process during friction stir vibration welding of magnesium alloys, Trans. Nonferrous Met. Soc. China (English Ed. 31 (2021) 2626–2650, https://doi.org/10.1016/S1003-6326(21)65681-9.

[35] B. Zahmatkesh, M.H. Enayati, A novel approach for development of surface nanocomposite by friction stir processing, Mater. Sci. Eng. 527 (2010) 6734–6740, https://doi.org/10.1016/j.msea.2010.07.024.

[36] V. Sharma, U. Prakash, B.V.M. Kumar, Surface composites by friction stir processing: a review, J. Mater. Process. Technol. 224 (2015) 117–134, https://doi.org/10.1016/j.jmatprotec.2015.04.019.

[37] M. Mehdizade, A.R. Eivani, M. Soltanieh, Characterization of the anodic oxide layer deposited on severely deformed and aged AA6063 aluminum alloy, J. Mater. Res. Technol. 15 (2021) 68–85, https://doi.org/10.1016/j.jmrt.2021.07.133.

[38] M. Mehdizade, A.R. Eivani, M. Soltanieh, Effects of reduced surface grain structure and improved particle distribution on pitting corrosion of AA6063 aluminum alloy, J. Alloys Compd. 838 (2020), 155464, https://doi.org/10.1016/j.jallcom.2020.155464.

[39] A. Bahmani, S. Arthanari, K.S. Shin, Achieving a high corrosion resistant and high strength magnesium alloy using multi directional forging, J. Alloys Compd. 856 (2021), 158077, https://doi.org/10.1016/j.jallcom.2020.158077.

[40] F. Liu, Y. Li, Z. Sun, Y. Ji, Corrosion resistance and tribological behavior of particles reinforced AZ31 magnesium matrix composites developed by friction stir processing, J. Mater. Res. Technol. 11 (2021) 1019–1030, https://doi.org/10.1016/j.jmrt.2021.01.071.

[41] L. Zhou, G.H. Li, G.D. Zha, F.Y. Shu, H.J. Liu, J.C. Feng, Effect of rotation speed on microstructure and mechanical properties of bobbin tool friction stir welded AZ61 magnesium alloy, Sci. Technol. Weld. Join. 23 (2018) 596–605, https://doi.org/10.1080/13621718.2018.1432098.

[42] P. Minárik, J. Veselý, J. Čížek, M. Zemková, T. Vlasák, T. Krajňák, J. Kubásek, R. Král, D. Hofman, J. Stráská, Effect of secondary phase particles on thermal stability of ultra-fine grained Mg-4Y-3RE alloy prepared by equal channel angular pressing, Mater. Char. 140 (2018) 207–216, https://doi.org/10.1016/j.matchar.2018.04.006.

[43] B. Bagheri, M. Abbasi, A. Abdollahzadeh, A.H. Kokabi, A comparative study between friction stir processing and friction stir vibration processing to develop magnesium surface nanocomposites, Int. J. Miner. Metall. Mater. 27 (2020) 1133–1146, https://doi.org/10.1007/s12613-020-1993-4.

[44] B. Bagheri, M. Abbasi, Development of AZ91/SiC surface composite by FSP: effect of vibration and process parameters on microstructure and mechanical characteristics, Adv. Manuf. 8 (2020) 82–96, https://doi.org/10.1007/s40436-019-00288-9.

[45] T. Al-Samman, G. Gottstein, Dynamic recrystallization during high temperature deformation of magnesium, Mater. Sci. Eng. 490 (2008) 411–420, https://doi.org/10.1016/j.msea.2008.02.004.

[46] X. Yang, H. Miura, T. Sakai, Dynamic evolution of new grains in magnesium alloy AZ31 during hot deformation, Mater. Trans. 44 (2003) 197–203, https://doi.org/10.2320/matertrans.44.197.

[47] X. yue Yang, Z. sheng Ji, H. Miura, T. Sakai, Dynamic recrystallization and texture development during hot deformation of magnesium alloy AZ31, Trans. Nonferrous Met. Soc. China (English Ed. 19 (2009) 55–60, https://doi.org/10.1016/S1003-6326(08)60228-9.

[48] L.B. Tong, X. Li, D.P. Zhang, L.R. Cheng, J. Meng, H.J. Zhang, Dynamic recrystallization and texture evolution of Mg-Y-Zn alloy during hot extrusion process, Mater. Char. 92 (2014) 77–83, https://doi.org/10.1016/j.matchar.2014.03.006.

[49] M. Mehdizade, M. Soltanieh, A.R. Eivani, Investigation of anodizing time and pulse voltage modes on the corrosion behavior of nanostructured anodic layer in commercial pure aluminum, Surf. Coating. Technol. 358 (2019) 741–752, https://doi.org/10.1016/j.surfcoat.2018.08.046.
[50] E. McCafferty, Introduction to Corrosion Science, Springer Science & Business Media, 2010.
[51] G. Song, A. Atrens, D. St John, X. Wu, J. Nairn, The anodic dissolution of magnesium in chloride and sulphate solutions, Corrosion Sci. 39 (1997) 1981–2004, https://doi.org/10.1016/S0010-938X(97)00090-5.
[52] R.L. Petty, A.W. Davidson, J. Kleinberg, The anodic oxidation of magnesium metal: evidence for the existence of unipositive magnesium, J. Am. Chem. Soc. 76 (1954) 363–366, https://doi.org/10.1021/ja01631a013.
[53] Z. Zhang, Z. Zhao, P. Bai, X. Li, B. Liu, J. Tan, X. Wu, In-situ monitoring of pitting corrosion of AZ31 magnesium alloy by combining electrochemical noise and acoustic emission techniques, J. Alloys Compd. 878 (2021), 160334, https://doi.org/10.1016/j.jallcom.2021.160334.
[54] M. Ascencio, M. Pekguleryuz, S. Omanovic, An investigation of the corrosion mechanisms of WE43 Mg alloy in a modified simulated body fluid solution: the influence of immersion time, Corrosion Sci. 87 (2014) 489–503.
[55] M. Ascencio, M. Pekguleryuz, S. Omanovic, An investigation of the corrosion mechanisms of WE43 Mg alloy in a modified simulated body fluid solution: the effect of electrolyte renewal, Corrosion Sci. 91 (2015) 297–310.
[56] W.M. Gan, M.Y. Zheng, H. Chang, X.J. Wang, X.G. Qiao, K. Wu, B. Schwebke, H. G. Brokmeier, Microstructure and tensile property of the ECAPed pure magnesium, J. Alloys Compd. 470 (2009) 256–262, https://doi.org/10.1016/j.jallcom.2008.02.030.
[57] G. Ben Hamu, D. Eliezer, L. Wagner, The relation between severe plastic deformation microstructure and corrosion behavior of AZ31 magnesium alloy, J. Alloys Compd. 468 (2009) 222–229.
[58] M. Alvarez-Lopez, M.D. Pereda, J.A. Del Valle, M. Fernandez-Lorenzo, M.C. Garcia-Alonso, O.A. Ruano, M.L. Escudero, Corrosion behaviour of AZ31 magnesium alloy with different grain sizes in simulated biological fluids, Acta Biomater. 6 (2010) 1763–1771, https://doi.org/10.1016/j.actbio.2009.04.041.
[59] M. Peron, P.C. Skaret, A. Fabrizi, A. Varone, R. Montanari, H.J. Roven, P. Ferro, F. Berto, J. Torgersen, The effect of Equal Channel Angular Pressing on the stress corrosion cracking susceptibility of AZ31 alloy in simulated body fluid, J. Mech. Behav. Biomed. Mater. 106 (2020), https://doi.org/10.1016/j.jmbbm.2020.103724.
[60] R. Ambat, N.N. Aung, W. Zhou, Evaluation of microstructural effects on corrosion behaviour of AZ91D magnesium alloy, Corrosion Sci. 42 (2000) 1433–1455, https://doi.org/10.1016/S0010-938X(99)00143-2.
[61] A. Heidarzadeh, S. Mironov, R. Kaibyshev, G. Çam, A. Simar, A. Gerlich, F. Khodabakhshi, A. Mostafaei, D.P. Field, J.D. Robson, A. Deschamps, P. J. Withers, Friction stir welding/processing of metals and alloys: a comprehensive review on microstructural evolution, Prog. Mater. Sci. 117 (2020), 100752, https://doi.org/10.1016/j.pmatsci.2020.100752.
[62] O. Kolednik, K. Unterweger, The ductility of metal matrix composites - relation to local deformation behavior and damage evolution, Eng. Fract. Mech. 75 (2008) 3663–3676, https://doi.org/10.1016/j.engfracmech.2007.08.011.
[63] Y.Z. Estrin, P.A. Zabrodin, I.S. Braude, T.V. Grigorova, N.V. Isaev, V.V. Pustovalov, V.S. Fomenko, S.E. Shumilin, Low-temperature plastic deformation of AZ31 magnesium alloy with different microstructures, Low Temp. Phys. 36 (2010) 1100–1106, https://doi.org/10.1063/1.3539781.
[64] Y. Estrin, A. Vinogradov, Extreme grain refinement by severe plastic deformation : a wealth of challenging science, Acta Mater. 61 (2013) 782–817, https://doi.org/10.1016/j.actamat.2012.10.038.
[65] P. Cavaliere, P.P. De Marco, Friction stir processing of AM60B magnesium alloy sheets, Mater. Sci. Eng. 462 (2007) 393–397.
[66] D.-T. Zhang, F. Xiong, W.-W. Zhang, Q.I.U. Cheng, W. Zhang, Superplasticity of AZ31 magnesium alloy prepared by friction stir processing, Trans. Nonferrous Metals Soc. China 21 (2011) 1911–1916.
[67] H. Waizy, J.M. Seitz, J. Reifenrath, A. Weizbauer, F.W. Bach, A. Meyer-Lindenberg, B. Denkena, H. Windhagen, Biodegradable magnesium implants for orthopedic applications, J. Mater. Sci. 48 (2013) 39–50, https://doi.org/10.1007/s10853-012-6572-2.
[68] B. Denkena, A. Lucas, Biocompatible magnesium alloys as absorbable implant materials–adjusted surface and subsurface properties by machining processes, CIRP Ann 56 (2007) 113–116.
[69] M. Salahshoor, Y. Guo, Biodegradable orthopedic magnesium-calcium (MgCa) alloys, processing, and corrosion performance, Materials 5 (2012) 135–155.
[70] R.B. Martin, Determinants of the mechanical properties of bones, J. Biomech. 24 (1991) 79–88, https://doi.org/10.1016/0021-9290(91)90379-2.
[71] G.O. Lease, F.G. Evans, Strength of human metatarsal bones under repetitive loading, J. Appl. Physiol. 14 (1959) 49–51, https://doi.org/10.1152/jappl.1959.14.1.49.
[72] H. Follet, G. Boivin, C. Rumelhart, P.J. Meunier, The degree of mineralization is a determinant of bone strength: a study on human calcanei, Bone 34 (2004) 783–789, https://doi.org/10.1016/j.bone.2003.12.012.
[73] S.N. Khan, R.M. Warkhedkar, A.K. Shyam, Analysis of hounsfield unit of human bones for strength evaluation, Procedia Mater. Sci. 6 (2014) 512–519, https://doi.org/10.1016/j.mspro.2014.07.065.
[74] L.-Y. Li, L.-Y. Cui, R.-C. Zeng, S.-Q. Li, X.-B. Chen, Y. Zheng, M.B. Kannan, Advances in functionalized polymer coatings on biodegradable magnesium alloys–a review, Acta Biomater. 79 (2018) 23–36.
[75] N.J. Ostrowski, B. Lee, A. Roy, M. Ramanathan, P.N. Kumta, Biodegradable poly (lactide-co-glycolide) coatings on magnesium alloys for orthopedic applications, J. Mater. Sci. Mater. Med. 24 (2013) 85–96.
[76] M. Razavi, M. Fathi, O. Savabi, D. Vashaee, L. Tayebi, Improvement of biodegradability, bioactivity, mechanical integrity and cytocompatibility behavior of biodegradable mg based orthopedic implants using nanostructured bredigite (Ca 7 MgSi 4 O 16) bioceramic coated via ASD/EPD technique, Ann. Biomed. Eng. 42 (2014) 2537–2550.
[77] L. Choudhary, R.S. Raman, J. Hofstetter, P.J. Uggowitzer, In-vitro characterization of stress corrosion cracking of aluminium-free magnesium alloys for temporary bio-implant applications, Mater. Sci. Eng. C 42 (2014) 629–636.
[78] T.J. Marrow, A. Bin Ahmad, I.N. Khan, S.M.A. Sim, S. Torkamani, Environment-assisted cracking of cast WE43-T6 magnesium, Mater. Sci. Eng. 387 (2004) 419–423.
[79] S. Jafari, S.E. Harandi, R.S. Raman, A review of stress-corrosion cracking and corrosion fatigue of magnesium alloys for biodegradable implant applications, JOM (J. Occup. Med.) 67 (2015) 1143–1153.
[80] M. Sozańska, A. Mościcki, B. Chmiela, Investigation of stress corrosion cracking in magnesium alloys by quantitative fractography methods, Arch. Metall. Mater. 62 (2017) 557–562.
[81] O. Hakimi, E. Aghion, J. Goldman, Improved stress corrosion cracking resistance of a novel biodegradable EW62 magnesium alloy by rapid solidification, in simulated electrolytes, Mater. Sci. Eng. C 51 (2015) 226–232.
[82] N. Winzer, A. Atrens, G. Song, E. Ghali, W. Dietzel, K.U. Kainer, N. Hort, C. Blawert, A critical review of the stress corrosion cracking (SCC) of magnesium alloys, Adv. Eng. Mater. 7 (2005) 659–693.
[83] Y. Li, K. Lietaert, W. Li, X.Y. Zhang, M.A. Leeflang, J. Zhou, A.A. Zadpoor, Corrosion fatigue behavior of additively manufactured biodegradable porous iron, Corrosion Sci. 156 (2019) 106–116.
[84] R.S. Raman, S. Jafari, S.E. Harandi, Corrosion fatigue fracture of magnesium alloys in bioimplant applications: a review, Eng. Fract. Mech. 137 (2015) 97–108.
[85] R.A. Antunes, M.C.L. de Oliveira, Corrosion fatigue of biomedical metallic alloys: mechanisms and mitigation, Acta Biomater. 8 (2012) 937–962.
[86] A.J. Griebel, J.E. Schaffer, Fatigue and corrosion fatigue of cold drawn WE43 wires, in: Magnes. Technol. 2015, Springer, 2015, pp. 303–307.
[87] Y.F. Zheng, X.N. Gu, F. Witte, Biodegradable metals, Mater. Sci. Eng. R Rep. 77 (2014) 1–34.